https://doi.org/10.1016/j.commatsci.2018.03.011

A quantitative phase-field model for crevice corrosion

Z.H. Xiao[a], S.Y. Hu[b], J.L. Luo[c], S.Q. Shi[a,*] and C.H. Henager Jr.[b]

[a] Department of Mechanical Engineering, the Hong Kong Polytechnic University, Hung Hom, Kowloon, Hong Kong

[b] Pacific Northwest National Laboratory, Richland, WA, USA

[c] Department of Chemical and Materials Engineering, University of Alberta, Edmonton, Canada

[*]Corresponding author. Email: mmsqshi@polyu.edu.hk

Abstract

A quantitative phase-field model is developed for the investigation of crevice corrosion of iron in salt water. Six types of ionic species and some associated chemical reactions have been considered. In addition to the transient distributions of ion concentrations and electric potential in the electrolyte, some physical and chemical properties related to corrosion, such as overpotential, pH value and corrosion rate, under different metal potentials are studied. Benchmarking of the phase-field model against a sharp interface model is conducted. The corrosion rates predicted by the models are in the same order of magnitudes with experimental results.

Keywords:

Phase-field modeling

Crevice corrosion

Iron

Nomenclature

A_c a constant related to the interface
c_i composition of species *i*
c_{ib} composition of species *i* close to the metal surface in the electrolyte
c_{1s} composition of Fe^{2+} at standard state in the electrolyte
C_i concentration of species *i* (mol/m^3)
C_{ib} concentration of species *i* close to the metal surface in the electrolyte (mol/m^3)
C_{1s} concentration of Fe^{2+} at standard state in the electrolyte (mol/m^3)
D_i diffusion coefficient of species *i* in the electrolyte (m^2/s)
D_m self-diffusion coefficient of iron atom (m^2/s)
D_{1r} diffusion coefficient of Fe^{2+} at a reference state when ϕ_M=-0.4V (m^2/s)
D_{ml} diffusion coefficient of Fe^{2+} within the interface (m^2/s)
E free energy functional (J)
E_b bulk free energy (J)
E_i interfacial energy (J)
f_b bulk free energy density (J /m^3)
f_i gradient free energy (J /m^3)
F Faraday's constant (96,485 C/mol)
j_1 flux of Fe^{2+} from metal into electrolyte (A/m^2)
j_{10} exchange current density of Fe^{2+} (A/m^2)
j_5 reduction rate of hydrogen ion at the anodic electrode (A/m^2)
j_{50} pre-exponential factor of j_5 (A·m^3/mol/m^2)
j_6 reduction rate of water ion on the anodic electrode (A/m^2)
k_{1B} backward reaction rate constant of the hydrolysis of Fe^{2+} (m^3/mol/s)
k_{2F} forward reaction rate constant of self-ionization of water (mol/m^3/s)
k_{2B} backward reaction rate constant of self-ionization of water (m^3/mol/s)
K_1 equilibrium constant of hydrolysis reaction of Fe^{2+} (mol/m^3)
K_2 self-ionization constant of water (mol^2/m^6)
$M(c_1)$ mobility of Fe^{2+} (mol·m^2/J/s)
n_x number of grids used in SIM
n_{xl} number of grids in electrolyte used in PFM
r coordinate in whole system domain (m)
R gas constant (8.314 J/mol/K)
T absolute temperature (K)
V_m molar volume of pure water (m^3/mol)
V_{Fe} molar volume of iron (m^3/mol)
x a dimensionless variable from 0 to 1
z_i charge of species *i*

Greek
α gradient energy coefficient (J·m^2/mol)
α_1 charge transfer coefficient of Fe^{2+}
α_5 charge transfer coefficient of H^+
α_6 charge transfer coefficient of reduction of water
ΔG the energy barrier between the electrolyte phase and metal phase
Δl grid size (m)
Δt time step (s)
η_a total overpotenital (V)
η_c concentration polarization overpotential close to

j_{60}	pre-exponential factor of j_6 (A/m^2)		metal-electrolyte interface (V)
j_{ml}	flux of Fe^{2+} under any electrode potential any given ϕ_M with $\phi_l + \eta_c$ setting to be 0 (A/m^2)	σ_s	surface tension (J/m^2)
		ϕ	electrostatic potential in electrolyte
		ϕ_M	electric potential in the metal (V)
j_{1r}	flux of Fe^{2+} at a reference state when ϕ_M=-0.4V (A/m^2)	ϕ_l	electric potential in the electrolyte close to metal-electrolyte interface (V)
k_{1F}	forward reaction rate constant of the hydrolysis of Fe^{2+} (s^{-1})	$\phi_{eq,M}$	standard electrode potential of iron (V)

1. Introduction

Crevice and pitting corrosion are localized corrosion in which there is intensive corrosion attack at localized sites on the metal surface inside crevices or pits. Those metals that resist corrosion by forming passive films, such as stainless steel, are vulnerable to crevice and pitting corrosion because of the breakdown of protective oxide film. In crevice corrosion for example, the anodic reactions mainly occur within the crevice and cathodic reactions mainly occur outside the crevice, and the cathodic region surface area is far larger than that of anodic region, which usually leads to pitting of the metal without large loss of metal mass by faster corrosion reaction inside the crevice. The propagation of pitting results in the degradation of the mechanical properties of the metallic material. Due to the extremely secluded geometry of crevice and pitting which is often hidden from view, crevice and pitting corrosion are very difficult to be detected.

There has been extensive investigation on crevice corrosion in the past decades. Two theories, i.e., critical crevice solution theory and IR drop theory have been proposed to describe crevice corrosion [1, 2]. In the critical crevice solution theory, it is assumed that the reaction of oxidants, such as oxygen, depletes the oxidant in the crevice. Due to the restrictive geometry of the crevice, the replenishing of oxidant from outside of the crevice

is too slow to maintain the cathodic reaction in the crevice. The anions, such as Cl^-, are transported into the crevice in order to neutralize the metal cation due to the dissolution of metal ions into the electrolyte. The hydrolysis of metal ions with water molecules generates H^+ ions that result in acidity in the crevice. When the concentrations of Cl^- and H^+ reach critical values, the passive film that protects the metal from the environment breaks down, and the accelerated corrosion in crevice starts. In the IR drop theory, it is assumed that there is an IR voltage drop in the solution produced by the separation of anodic and cathodic reactions. The IR voltage drop is proportional to the ionic current (I) flowing through a solution with a resistance (R) determined by the length of the current path, the cross-section area of crevice and the conductivity of solution in the crevice. If the voltage IR drop is large enough, the electrode potential in the crevice will shift from the passive region into the active region in the polarization curve, corresponding to the occurrence of crevice corrosion. A number of mathematical and numerical models based on the critical crevice solution theory [3-9], IR drop theory [10] and both theories [11, 12], have been developed for crevice corrosion.

Crevice corrosion of an active metal is a very complex phenomenon and involves multiscale physical and chemical processes. The metal ions get into electrolyte in the dissolution process of metal under the gradient of electrochemical potential via an electrical double layer (DL) which separates the metal phase from the electrolyte phase. There is net electric charge which forms a dipole in the DL (a layer with a thickness in the order of nanometers), in which the electrochemical reactions mainly occur. The metal ion and other ions may chemically react with each other and are transported in the crevice solution over a typical length scale of millimeters. The solution part extent is much larger than the

thickness of DL. The electrical potential gradients and composition gradients of metal ions are very large in DL and relatively small in the crevice solution. Due to the presence of net electrical charge, thin DL, and huge drop of electrical potential and concentration of metal ion across the DL, the numerical simulation of physical and chemical processes within the vicinity of DL is difficult. Thus, the electrochemical reactions inside the DL have not been taken into account in the reported mathematical and numerical models for crevice corrosion. And, for simplicity, the electrolyte was usually treated as electrically neutral in those studies.

During crevice corrosion, the interface between metal and solution moves due to the dissolution of metal, and new phases, such as hydrogen gas and/or corrosion products might form if the crevice solution is supersaturated [1]. Both the interface migration and new phase formation modify the crevice geometry and physical environment, which, in turn, influence the local chemical potential and the crevice corrosion kinetics. Thus, the interface should be treated as a moving boundary for a quantitative model of crevice corrosion. A moving boundary is difficult to deal with, especially for crevices with complex topological geometries. The traditional way to deal with the moving boundary problem was to use sharp interface model (SIM) in which the position of interface was tracked explicitly in the simulations. To model crevice corrosion or pitting corrosion, some complex algorithms of moving mesh were developed to track the moving interface using some numerical techniques, such as finite element method [8, 13-18], finite volume method [19], boundary element method [20-22] and arbitrary Lagrangian–Eulerian model [23]. It is difficult to successfully cope with both the multiphysics calculation and the smooth moving interface of arbitrary crevice shapes while maintaining conservation of mass and

electroneutrality. Special methods are needed to guarantee the conservation of mass and electroneutrality when the interface moves [19].

In the past two decades, phase-field methods (PFM) based on a diffusive interface concept without the need of tracking the interface position explicitly [24, 25], have advanced very rapidly. Significant phase-field modeling work has been done on electrochemical systems. PFM offers an alternative method to model crevice or pitting corrosion. Guyer et al. developed a one-dimensional PFM of an electrochemical system that can handle both the electro-dissolution and electro-deposition, including the net charges present in the interface by incorporating the Poisson equation into the model [26, 27]. Basing on Guyer's model, Gathright et al. built phase-field model to simulate solid-electrolyte gas sensor [28] and electrochemical impedance spectroscopy experiments [29]. However, due to the restriction of electric double layer size, the model can only handle systems with a size about tens of nanometers. Later on, PFM was implemented on the studies of thermal oxidation [30-33], electrochemical processes[34], especially the reverse process of corrosion, such as metal refining [35], electro-deoxidation [36] and electro-deposition [37-40].

One recent attempt has been made to use PFM to study corrosion [41, 42]. W. Mai et al. studied activation-controlled and diffusion controlled pitting corrosion processes, electropolishing processes and stress corrosion cracking. The chemical reaction between different types of ions and the distribution of electric potential in electrolytes, hence the electromigration of charged particles, were not taken into account in their model, which are very important factors in the corrosion process. In their recent work [43], W. Mai et al. proposed a 2D model to study the influence of oxygen concentration and electric potential distribution in electrolyte to the pitting corrosion process, and a 1D model considering the

distribution of several ion species concentration and electric potential in electrolytes to study a 1D pencil electrode corrosion. However the effect of metal ion concentration in the electrolyte on polarizing the total overpotential was not considered in their model, which is very important for the corrosion process, especially for modeling the diffusion controlled corrosion process.

In this work, we propose a quantitative PFM for the study of crevice (or pitting) corrosion, which not only considers the overpotential via the Butler-Volmer equation, but also incorporates the electric potential distribution and chemical reactions between different types of ions in the electrolyte. The model system is one with iron immersed in 3% *NaCl* solution, the same system studied by Sharland et al. [6, 7] and Turnbull et al. [4]. It should be noted that both Sharland and Turnbull's work assumed steady-state corrosion kinetics, while our model is fully time-dependent. The work described below ignores the formation of passive films, and the effect of passive film on localized corrosion will be studied in the future. For the convenience of verifying our PFM against the SIM and simplification of calculation, one-dimensional simulation is carried out.

2. Model description

Similar to Sharland's work [6], our model assumes that the corrosion only happens at the tip of a crevice, meaning that the side wall of a crevice is passivated. For the system of iron in salt water, we consider six types of ions and the following ion-containing chemical reactions taking place in the electrolyte.

$$Fe^{2+} + H_2O \leftrightarrow FeOH^+ + H^+ \tag{1}$$

$$H_2O \leftrightarrow OH^- + H^+ \tag{2}$$

Here, we assume that there is no passive film formed during corrosion. The six ions are Fe^{2+}, $FeOH^{+}$, Cl^{-}, Na^{+}, H^{+}, OH^{-}. The concentrations of these ions are denoted as follows. $\left[Fe^{2+}\right]=C_1$, $\left[FeOH^{+}\right]=C_2$, $\left[Cl^{-}\right]=C_3$, $\left[Na^{+}\right]=C_4$, $\left[H^{+}\right]=C_5$, and $\left[OH^{-}\right]=C_6$. The composition c_i of the i^{th} ion type is related to the corresponding concentration C_i by $c_i=C_iV_m$, where V_m is the molar volume of pure water. Fluid convection is not considered in this model due to the occluded crevice geometry. The electrode potentials are measured on the standard hydrogen electrode (SHE) scale in this work.

2.1. Phase-field model

The governing equation of Fe^{2+} is the Cahn-Hilliard equation augmented with electro-migration term and chemical reaction terms. The governing equations of the other five ion species are the Nernst-Planck equations with chemical reaction terms. They are written as follows:

$$\frac{\partial c_1}{\partial t}=\nabla\left\{M\left(c_1\right)\nabla\frac{\delta E}{\delta c_1}\right\}-k_{1F}c_1+k_{1B}c_2c_5/V_m \tag{3}$$

$$\frac{\partial c_2}{\partial t}=D_2\nabla^2c_2+\nabla\left[z_2Fc_2\frac{D_2}{RT}\nabla\phi\right]+k_{1F}c_1-k_{1B}c_2c_5/V_m \tag{4}$$

$$\frac{\partial c_3}{\partial t}=D_3\nabla^2c_3+\nabla\left[z_3Fc_3\frac{D_3}{RT}\nabla\phi\right] \tag{5}$$

$$\frac{\partial c_4}{\partial t}=D_4\nabla^2c_4+\nabla\left[z_4Fc_4\frac{D_4}{RT}\nabla\phi\right] \tag{6}$$

$$\frac{\partial c_5}{\partial t}=D_5\nabla^2c_5+\nabla\left[z_5Fc_5\frac{D_5}{RT}\nabla\phi\right]+k_{1F}c_1-k_{1B}c_2c_5/V_m+k_{2F}V_m-k_{2B}c_5c_6/V_m \tag{7}$$

$$\frac{\partial c_6}{\partial t}=D_6\nabla^2c_6+\nabla\left[z_6Fc_6\frac{D_6}{RT}\nabla\phi\right]+k_{2F}V_m-k_{2B}c_5c_6/V_m \tag{8}$$

and the net charge in the electrolyte is assumed to be zero, which means that the electroneutrality condition is applied, and

$$\sum_{i=1}^{6} z_i c_i = 0 \tag{9}$$

where D_i (i=1,2,…,6) is the diffusion coefficient of species i; z_i (i=1,2,…,6) the charge of species i (z_1 = +2, z_2 = +1, z_3 = -1, z_4 = +1, z_5 = +1, z_6 = -1); F the Faraday constant; ϕ the electrostatic potential in electrolyte; R the gas constant; and T the absolute temperature. k_{1F} and k_{2F} are the forward reaction rate constants of the chemical reactions (1) and (2), respectively, while k_{1B} and k_{2B} are backward reaction rate constants of reactions (1) and (2), respectively. The reaction rates are related to the equilibrium constants as

$$K_1 = \frac{k_{1F}}{k_{1B}} \tag{10}$$

$$K_2 = \frac{k_{2F}}{k_{2B}} \tag{11}$$

At equilibrium, there are following relations for the state of reactions (1) and (2)

$$K_1 = \frac{C_2 C_5}{C_1} = \frac{c_2 c_5}{V_m c_1} \tag{12}$$

$$K_2 = C_5 C_6 = \frac{c_5 c_6}{V_m V_m} \tag{13}$$

It should be noted that the Cahn-Hilliard equation (3) apply to the whole system, including the metal and electrolyte. The other equations from (4) to (9) apply only to the electrolyte.

The Cahn-Hilliard equation (3) should be able to be reduced to the Nernst-Planck equation in the electrolyte as used in the sharp interface model as

$$\frac{\partial c_1}{\partial t} = D_1 \nabla^2 c_1 + \nabla \left\{ z_1 F c_1 \frac{D_1}{RT} \nabla \phi \right\} - k_{1F} c_1 + k_{1B} c_2 c_5 / V_m \tag{14}$$

where E in the Cahn-Hilliard equation (3) is the free energy functional, which includes the bulk free energy E_b, interfacial energy E_i and electrostatic energy E_e as,

$$E=E_b+E_i+E_e=\int\left[\, f_b\left(c_1\right)+\, f_i+\, f_e\,\right]dV \tag{15}$$

where $f_b(c_1)$ is the bulk free energy density. For a regular solution

$$f_b\left(c_1\right)=RT\left[\, c_1\ln c_1+\left(1-c_1\right)\ln\left(1-c_1\right)+c_1\left(1-c_1\right)\frac{\Delta G}{RT}\,\right] \tag{16}$$

which is a double well function with two local minima at c_{1s} and 1-c_{1s} representing the electrolyte phase and metal phase, respectively. c_{1s} is the composition of Fe^{2+} at the standard state in the electrolyte with a value of 1.8×10^{-2}, corresponding to 1M. ΔG is the energy barrier between the electrolyte phase and the metal phase. Since the value of ΔG is not available from the literature, it was chosen to make sure that the two local minima are at c_{1s} and 1-c_{1s} ≈1, respectively.

f_i is the gradient free energy at the metal-electrolyte interface written as

$$f_i=\alpha\left(\nabla c_1\right)^2 \tag{17}$$

where α is the gradient energy coefficient related to the surface tension σ_s. It is written as

$$\alpha=A_c\frac{\left(\sigma_s V_m\right)^2}{RT} \tag{18}$$

where A_c is a constant related to the interfacial width and the bulk free energy density.

f_e is the electrostatic energy density, which only applies in the electrolyte portion. It is written as

$$f_e=z_1Fc_1\phi \tag{19}$$

In this PFM, the Cahn-Hilliard equation (3) is used to automatically track the interface between the metal and electrolyte, while Neumann boundary conditions are assigned for the Nernst -Planck equations of other five species.

The mobility $M(c_1)$ is a piecewise function. In the electrolyte, the mobility is

$$M\left(c_1\right)=\frac{1}{RT}\frac{D_1}{2\ln c_1+1/\left[c_1\left(1-c_1\right)\right]} \tag{20}$$

where D_1 is the diffusion coefficient of metal ion in the electrolyte, same as in the SIM. This expression of mobility $M(c_1)$, when combined with the expression of bulk free energy density (16) and the electrostatic energy density (19), guarantees that the Cahn-Hilliard equation (3) will reduce to Eq. (14) in the electrolyte.

In the metal, the mobility is

$$M\left(c_1\right)=\frac{D_m}{RT} \tag{21}$$

where D_m is the diffusion coefficient of metal atom in the metal.

Within the metal-electrolyte interface, the mobility is

$$M\left(c_1\right)=\frac{1}{RT}\frac{D_{ml}}{2\ln c_{1s}+1/\left[c_{1s}\left(1-c_{1s}\right)\right]} \tag{22}$$

where D_{ml} is the diffusion coefficient of the metal ion within the interface, which controls the interface velocity in the metal dissolution process. It is related to the metal ion flux from the metal into the electrolyte j_1 as determined by total polarization overpotential η_a via the Butler-Volmer equation

$$j_1 = j_{10}\left[\exp\left((1-\alpha_1)z_1F\eta_a/RT\right)-\exp\left(-\alpha_1 z_1F\eta_a/RT\right)\right] \tag{23}$$

where j_{10} is the exchange current density. Its value typically ranges from 10^{-4} to 10^{-2} Am^{-2} around pH 7 [44, 45]. Here, we choose $j_{10} = 2.7\times10^{-3}\,\mathrm{Am}^{-2}$ [44, 45]. α_1 is the charge transfer coefficient. The total overpotential, η_a, is determined by

$$\eta_a = \phi_M - \phi_l - \phi_{eq,M} - \eta_c \tag{24}$$

where ϕ_M is the electric potential in the metal; ϕ_l is the electric potential in the electrolyte close to the metal-electrolyte interface; $\phi_{eq,M}$ the equilibrium potential at standard condition which is -0.44V (SHE) for iron. We define the concentration polarization at crevice tip, η_c, with respect to the concentration at standard state instead of the concentration at bulk solution as

$$\eta_c = \frac{RT}{z_1 F}\ln\frac{C_{1b}}{C_{1s}} = \frac{RT}{z_1 F}\ln\frac{c_{1b}}{c_{1s}} \tag{25}$$

At standard condition, C_{1s}= 1M and c_{1s} = $C_{1s}V_m$, which is the first local minimum representing the electrolyte phase in the bulk free energy f_b. C_{1b} (c_{1b}) is the concentration (composition) of Fe^{2+} close to metal surface in the electrolyte. $\phi_{eq,M}$ + ϕ_l + η_c, instead of $\phi_{eq,M}$ + η_c, is the equilibrium potential because there is electric potential distribution in the electrolyte.

ϕ_l and η_c change with time during the corrosion process. For convenience, we start the simulation with the initial condition ϕ_l = -η_c. Corrosion takes place when η_a> 0. The system reaches equilibrium when the overpotential η_a tends to be zero. Since Tafel equation is not valid in low overpotential region, the Butler-Volmer equation is used to define the flux.

In order to determine the value of D_{ml}, we assume,

$$D_{ml} = D_{1r} \frac{j_{ml}}{j_{1r}} \tag{26}$$

where D_{1r} and j_{1r} are diffusion coefficient and flux of Fe^{2+}, respectively, at a reference state when ϕ_M=-0.4V, corresponding to a total overpotential η_a of 0.136V obtained by calibration simulation. j_{1r} can be obtained by substituting η_a into Eq. (23). D_{1r} is set to a value of 5×10^{-15} m^2/s by calibrating the PFM against the SIM, see section 3.1. j_{ml} is the metal ion flux under any electrode potential ϕ_M, which can be obtained by substituting corresponding η_a into Eq. (23). Since D_{1r} and j_{1r} are constants, the value of D_{ml} will change with the total overpotential η_a in the simulation process.

In order to verify our PFM against the SIM, same as in Sharland's work [6, 7], we assume that the geometrical structure of the crevice is a parallel-sided slot in the metal and that the two crevice walls are passivated. Thus, the problem is reduced to a simplified one-dimensional problem with the corrosion only occurring at the crevice tip as shown in Fig. 1.

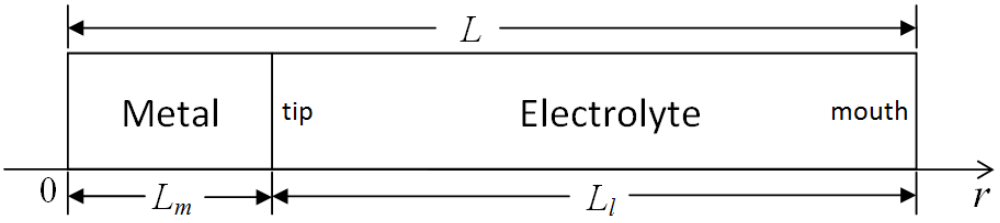

Fig. 1. The one dimension geometry of crevice. L is the length of the whole system, which includes the metal and the electrolyte with a length L_m and L_l, respectively.

In one dimension, the Cahn-Hilliard equation is rewritten as

$$\frac{\partial c_1}{\partial t} = \frac{\partial}{\partial r}\left\{ M\left(c_1\right)\frac{\partial}{\partial r}\left[RT\ln\frac{c_1}{1-c_1} - RT(1-2c_1)\ln c_{1s} - 2\alpha\nabla^2 c_1 \right]\right\} + \frac{\partial}{\partial r}\left\{ z_1 F c_1 \frac{D_1}{RT}\frac{\partial \phi}{\partial r}\right\} - k_{1F}c_1 + k_{1B}c_2 c_5 / V_m \tag{27}$$

where r is given as $0 \leq r \leq L$. Electro-migration and chemical reaction only apply in the electrolyte portion, which means that there is no distribution of electrostatic potential or of the other five ion species in the metal portion.

In order to solve the one-dimensional Eqs. (4)-(9) with a moving boundary at the metal-electrolyte interface, the following coordinate transformation is applied (Appendix I).

$$X(t) = L_l(t)x \text{ , } 0<x<1 \tag{28}$$

where x is a dimensionless variable, L_l is the length of electrolyte portion which varies with time as the corrosion process proceeds. It is possible to avoid such transformation in 2D or 3D if one considers one domain for all ionic species in the modeling, that is, the domain includes both metal and electrolyte. In this work, the main objective is to verify and validate the framework of PFM for corrosion modeling as compared to SIM. The coordinate transformation is for the convenience of comparison of the results obtained by PFM and SIM in 1D.

Eqs. (4)-(9) in the new coordinate after substituting Eq. (9) into Eq. (5) to cancel c_3 are rewritten as

$$\frac{\partial c_2(x,t)}{\partial t} + \frac{x}{L_l}\frac{dL_l}{dt}\frac{\partial c_2(x,t)}{\partial x} = \frac{D_2}{{L_l}^2}\frac{\partial^2 c_2(x,t)}{\partial x^2} + \frac{z_2 D_2 F}{RT{L_l}^2}\frac{\partial}{\partial x}\left(c_2 \frac{\partial \phi(x,t)}{\partial x}\right) + k_{1F}c_1 - k_{1B}c_2 c_5 / V_m \tag{29}$$

$$\begin{aligned}
&\frac{z_1(D_1-D_3)}{L^2}\frac{\partial^2 c_1(x,t)}{\partial x^2}+\frac{z_2(D_2-D_3)}{L^2}\frac{\partial^2 c_2(x,t)}{\partial x^2}+\frac{z_4(D_4-D_3)}{L^2}\frac{\partial^2 c_4(x,t)}{\partial x^2}\\
&+\frac{z_5(D_5-D_3)}{L^2}\frac{\partial^2 c_5(x,t)}{\partial x^2}+\frac{z_6(D_6-D_3)}{L^2}\frac{\partial^2 c_6(x,t)}{\partial x^2}\\
&+\frac{F}{L^2RT}\frac{\partial}{\partial x}\{[z_1(z_1D_1-z_3D_3)c_1(x,t)+z_2(z_2D_2-z_3D_3)c_2(x,t)+z_4(z_4D_4-z_3D_3)c_4(x,t)\\
&+z_5(z_5D_5-z_3D_3)c_5(x,t)+z_6(z_6D_6-z_3D_3)c_6(x,t)]\frac{\partial\phi(x,t)}{\partial x}\}\\
&+(z_5+z_6)k_{2F}V_m+(z_1-z_2-z_5)k_{1B}c_2c_5/V_m-(z_5+z_6)k_{2B}c_5c_6/V_m-(z_1-z_2-z_5)k_{1F}c_1\\
&=0
\end{aligned} \tag{30}$$

$$\frac{\partial c_4(x,t)}{\partial t}+\frac{x}{L_l}\frac{dL_l}{dt}\frac{\partial c_4(x,t)}{\partial x}=\frac{D_4}{L_l^{\,2}}\frac{\partial^2 c_4(x,t)}{\partial x^2}+\frac{z_4D_4F}{RTL_l^{\,2}}\frac{\partial}{\partial x}\left(c_4\frac{\partial\phi(x,t)}{\partial x}\right) \tag{31}$$

$$\begin{aligned}
\frac{\partial c_5(x,t)}{\partial t}+\frac{x}{L_l}\frac{dL_l}{dt}\frac{\partial c_5(x,t)}{\partial x}&=\frac{D_5}{L_l^{\,2}}\frac{\partial^2 c_5(x,t)}{\partial x^2}+\frac{z_5D_5F}{RTL_l^{\,2}}\frac{\partial}{\partial x}\left(c_5\frac{\partial\phi(x,t)}{\partial x}\right)\\
&+k_{2F}V_m-k_{2B}c_5c_6/V_m+k_{1F}c_1-k_{1B}c_2c_5/V_m
\end{aligned} \tag{32}$$

$$\begin{aligned}
\frac{\partial c_6(x,t)}{\partial t}+\frac{x}{L_l}\frac{dL_l}{dt}\frac{\partial c_6(x,t)}{\partial x}&=\frac{D_6}{L_l^{\,2}}\frac{\partial^2 c_6(x,t)}{\partial x^2}+\frac{z_6D_6F}{RTL_l^{\,2}}\frac{\partial}{\partial x}\left(c_6\frac{\partial\phi(x,t)}{\partial x}\right)\\
&+k_{2F}V_m-k_{2B}c_5c_6/V_m
\end{aligned} \tag{33}$$

The boundary conditions for the Cahn-Hilliard equation (27) are

$$\begin{aligned}
&\left.\frac{\partial c_1(r,t)}{\partial r}\right|_{r=0}=0,\ c_1(r,t)\big|_{r=L}=1.8\times10^{-9},\ \left.\frac{\partial^2 c_1(r,t)}{\partial r^2}\right|_{r=L}=0,\\
&\left.\frac{\partial^3 c_1(r,t)}{\partial r^3}\right|_{r=L}=0
\end{aligned} \tag{34}$$

where the first condition is the requirement that there are no metal ions entering into the system from the left boundary (r = 0) to influence the motion of the metal-electrolyte interface. For the second condition, the composition of metal ion at the crevice mouth is set to be a very small value of 1.8×10^{-9}, instead of zero, due to the logarithm term used in

the bulk free energy. The third and fourth conditions are the requirement for the Cahn-Hilliard equation (27) to reduce to the Nernst-Planck equation at the boundary $r = L$.

The Neumann boundary conditions are applied at the crevice tip where $x = 0$ for the governing equations of other species and electrostatic potential,

$$\left.\frac{\partial c_2(x,t)}{\partial x}\right|_{x=0} + \frac{z_2 F}{RT} c_2(x,t) \left.\frac{\partial \phi(x,t)}{\partial x}\right|_{x=0} = 0 \tag{35}$$

$$\begin{aligned} &\frac{F}{RT}[z_1(z_3 - z_1)c_1(x,t) + z_2(z_3 - z_2)c_2(x,t) + z_4(z_3 - z_4)c_4(x,t) \\ &+ z_5(z_3 - z_5)c_5(x,t) + z_6(z_3 - z_6)c_6(x,t)] \left.\frac{\partial \phi(x,t)}{\partial x}\right|_{x=0} \\ &= \left(\frac{j_1}{D_1} + \frac{j_5}{D_5} + \frac{j_6}{D_6}\right)\frac{V_m L}{F} \end{aligned} \tag{36}$$

$$\left.\frac{\partial c_4(x,t)}{\partial x}\right|_{x=0} + \frac{z_4 F}{RT} c_4(x,t) \left.\frac{\partial \phi(x,t)}{\partial x}\right|_{x=0} = 0 \tag{37}$$

$$\left.\frac{\partial c_5(x,t)}{\partial x}\right|_{x=0} + \frac{z_5 F}{RT} c_5(x,t) \left.\frac{\partial \phi(x,t)}{\partial x}\right|_{x=0} = \frac{-j_5 V_m L_l}{z_5 F D_5} \tag{38}$$

$$\left.\frac{\partial c_6(x,t)}{\partial x}\right|_{x=0} + \frac{z_6 F}{RT} c_6(x,t) \left.\frac{\partial \phi(x,t)}{\partial x}\right|_{x=0} = \frac{-j_6 V_m L_l}{z_6 F D_6} \tag{39}$$

where j_5 is the reduction rate of hydrogen ion at the anodic electrode due to the reaction

$$H^+ + e^- \rightarrow \frac{1}{2} H_2 \tag{40}$$

and j_5 is given by

$$j_5 = j_{50} C_5 \exp\left(\alpha_5 F \eta_a / RT\right) \tag{41}$$

where $j_{50} = -2 \times 10^{-3}\,\mathrm{A \cdot m^3 / mol \cdot m^2}$, α_5 = -0.5, C_5 is the concentration of H^+ in the electrolyte close to anodic electrode [4].

j_6 is the reduction rate of water on the anodic electrode due to the reaction

$$H_2O + e^- \rightarrow H + OH^- \tag{42}$$

And it is given by

$$j_6 = j_{60} \exp\left(\alpha_6 F \eta_a / RT\right) \tag{43}$$

where $j_{60} = 8\times10^{-10}\,\mathrm{A/m^2}$, α_6 = -0.5 [4].

Dirichlet boundary conditions are applied at the crevice mouth where x = 1 as follows:

$$c_2(x,t)\big|_{x=1} = \frac{K_1 V_m c_1}{c_5} \tag{44}$$

$$\phi(x,t)\big|_{x=1} = 0 \tag{45}$$

$$c_4(x,t)\big|_{x=1} = 9.24\times10^{-3}\left(0.513\mathrm{M}\right) \tag{46}$$

Which corresponds to a 3% *NaCl* solution, and

$$c_5(x,t)\big|_{x=1} = 1.8\times10^{-9}\left(10^{-7}\mathrm{M}\right) \tag{47}$$

$$c_6(x,t)\big|_{x=1} = 1.8\times10^{-9}\left(10^{-7}\mathrm{M}\right) \tag{48}$$

where the values in the brackets are concentrations.

The initial composition of Fe^{2+} is set to 1 uniformly in the metal and which drops to $c_1(x,t)\big|_{x=0,t=0}$ in the electrolyte via a Heaviside function. $c_1(x,t)\big|_{x=0,t=0}$ is selected to be far smaller than c_{1s}. Within the electrolyte, the Fe^{2+}composition is assumed to be

$$c_1(x,t)\big|_{t=0} = c_1(x,t)\big|_{x=0,t=0} - x\left[c_1(x,t)\big|_{x=0,t=0} - c_1(r,t)\big|_{r=L}\right] \tag{49}$$

$c_1(r,t)\big|_{r=L}$ is the boundary condition of the metal ion at crevice mouth. The initial values of other species and electric potential are

$$c_2(x,t)\big|_{t=0} = \frac{K_1 V_m\, c_1(x,t)\big|_{t=0}}{c_5(x,t)\big|_{t=0}} \tag{50}$$

$$\phi(x,t)\big|_{t=0} = \phi(x,t)\big|_{x=0,t=0} - x\left[\phi(x,t)\big|_{x=0,t=0} - \phi(x,t)\big|_{x=1}\right] \tag{51}$$

$$c_4(x,t)\big|_{t=0} = c_4(x,t)\big|_{x=1} \tag{52}$$

$$c_5(x,t)\big|_{t=0} = c_5(x,t)\big|_{x=1} \tag{53}$$

$$c_6(x,t)\big|_{t=0} = c_6(x,t)\big|_{x=1} \tag{54}$$

where $\phi(x,t)\big|_{x=0,t=0} = - RT\ln(c_{1b}/c_{1s})/F/z_1$, which makes the initial value of $\phi_l + \eta_c$ equal to 0. The value of c_3 can be obtained at any time and any position in the electrolyte according to Eq. (9).

2.2. Sharp interface model

In this model all six species are governed by the Nernst-Planck equations. The Nernst-Planck equation (14) for metal ions in the transformed coordinate is written as,

$$\frac{\partial c_1(x,t)}{\partial t} + \frac{x}{L_l}\frac{dL_l}{dt}\frac{\partial c_1(x,t)}{\partial x} = \frac{D_1}{L_l^2}\frac{\partial^2 c_1(x,t)}{\partial x^2} + \frac{z_1 D_1 F}{RTL_l^2}\frac{\partial}{\partial x}\left(c_1\frac{\partial \phi(x,t)}{\partial x}\right) - k_{1F}c_1 + k_{1B}c_2c_5/V_m \tag{55}$$

L_l is determined by the following equation,

$$\frac{dL_l(t)}{dt} = \frac{j_1 V_{Fe}}{z_1 F} \tag{56}$$

where V_{Fe} is molar volume of iron, j_1 the flux of Fe^{2+} from metal into the electrolyte. The governing equations for the other species and electric potential are the same Eqs. (29)-(33).

The boundary conditions for the Nernst-Planck equations (55) at crevice tip and mouth are written as

$$\left.\frac{\partial c_1(x,t)}{\partial x}\right|_{x=0} + \frac{z_1 F}{RT} c_1(x,t) \left.\frac{\partial \phi(x,t)}{\partial x}\right|_{x=0} = \frac{-j_1 V_m L_l}{z_1 F D_1} \tag{57}$$

$$c_1(x,t)\big|_{x=1} = 0 \tag{58}$$

The boundary conditions for the other species and electric potential are the same as those given in the previous section.

Since there is only one electrolyte region to be considered in the sharp interface model, the initial condition for Fe^{2+} is set only in the electrolyte, which is the same as Eq. (49). The initial conditions for other species are the same as those given in the previous section.

2.3 Material parameters and model parameters

Parameters are given in Table 1. Values for k_{1F} and k_{1B} were not available. The value of K_1 is taken from Ref. [46, 47]. Tests on k_{1F} and k_{1B} showed that their values will not strongly affect the final results. Thus, we simply set k_{1F} = 1.0 s^{-1}. Then, according to Eq. (10), we can get k_{1B} = 3.162×10^9 1/(M·s) = 3.162×10^6 m^3/(mol·s).

Table 1

Values of parameters.

Parameter	Value
T	298 K
σ_s	0.2 J/m^2
V_m	1.8×$10^{-5}$$m^3$/mol
V_{Fe}	7.0923×10^{-6} m^3/mol
A_c	0.5×10^8
c_{1s}	1.8×10^{-2}
ΔG	1.027×10^4 J/mol
$\phi_{eq,M}$	-0.44V (SHE)
K_1 [a]	3.162×10^{-7}mol/m^3
K_2 [b]	1×10^{-8} (mol/m^3)^2

k_{1F}	$1.0\ s^{-1}$
k_{1B}	$3.162\times10^{6}\ m^3/(mol\cdot s)$
k_{2F} [b]	$1.4\ mol/(m^3\cdot s)$
k_{2B} [b]	$1.4\times10^{8}\ m^3/(mol\cdot s)$
j_{10} [c]	$2.7\times10^{-3}\ Am^{-2}$
j_{50} [d]	$-2\times10^{-3}\ Am^3/mol/m^2$
j_{60} [d]	$8\times10^{-10}\ Am^{-2}$
α_1 [d]	0.5
α_5 [d]	-0.5
α_6 [d]	-0.5
D_1 [d]	$1\times10^{-9}m^2/s$
D_2 [d]	$1\times10^{-9}m^2/s$
D_3 [d]	$1\times10^{-9}m^2/s$
D_4 [d]	$1\times10^{-9}m^2/s$
D_5 [d]	$9.3\times10^{-9}m^2/s$
D_6 [d]	$5.\ 3\times10^{-9}m^2/s$
D_m	$3\times10^{-13}m^2/s$
D_{1r}	$1.5\times10^{-15}\ m^2/s$
L	$2.5\times10^{-3}m$
L_l	$2\times10^{-3}m$
L_m	$0.5\times10^{-3}m$
n_x	200
n_{xl}	200
Δl	$10^{-5}m$
Δt	$2\times10^{-4}s$

[a] Ref. [46, 47]
[b] Ref. [48, 49]
[c] Ref. [44, 45]
[d] Ref. [4]

Since L_l and L_m change with time, their values in the table are initial values. In the SIM, the whole domain x is from 0 to 1, which is divided into a fixed number of grids n_x. While in the PFM, the grids number n_{xl} in electrolyte part increases with L_l. Thus, a mapping of the values of compositions and electric potential between the two types of grids is needed, see Appendix II for details. The value of n_{xl} in the table is an initial value. The grid size in PFM is Δl. The time step Δt used in both models is the same.

The Crank-Nicolson numerical method is used to solve the Nernst-Planck equations. For the numerical solutions of the Cahn-Hilliard equation, the forward Euler method is used

for the time derivatives, while the centered finite difference method is used to approximate the Laplacican.

3. Results and discussion

In order to compare the results obtained using the two models, we studied several cases under the same initial and boundary conditions. For corrosion to occur, $\eta_a > 0$ is required according to Eq. (23). In all the simulations of this work, the initial value of ϕ_l is set to $-\eta_c$. Thus, $\phi_M > \phi_{eq,M}$ is required for corrosion to proceed.

3.1. The comparison study at ϕ_M = -0.4V

Since we do not know the parameter, D_{ml}, for the interface velocity in the PFM, a calibration study between PFM and SIM was carried out to evaluate the value of diffusion coefficient, D_{ml}, according to the expression (26). Fig. 2 shows the simulation results obtained from SIM and PFM by setting $D_{1r} = 5\times10^{-15}$ m^2/s under ϕ_M = -0.4V, which corresponds to an initial overpotential, η_a, 0.04V. Then, we use this D_{1r} to find D_{ml} under other electrode potentials according to Eq. (26). The overpotential, η_a, changes with time, see Eq. (24), because the electric potential, ϕ_l, and metal ion concentration, C_{1b}, close to the metal surface in the electrolyte change with time. Comparing the results obtained by SIM and PFM indicates that the value of 5×10^{-15} m^2/s for D_{1r} is a good choice for PFM.

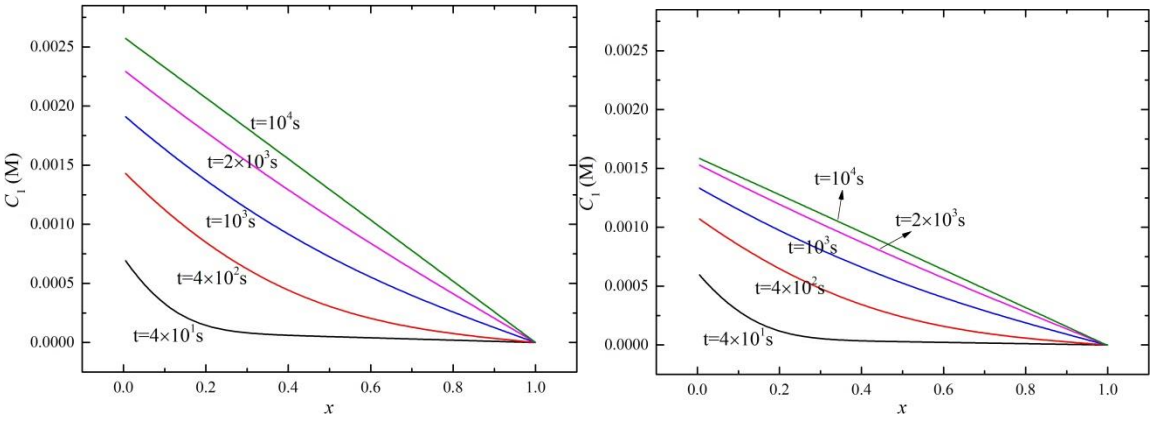
C_1 (M)
x
t=10^4s
t=2×10^3s
t=10^3s
t=4×10^2s
t=4×10^1s

(a) (b)

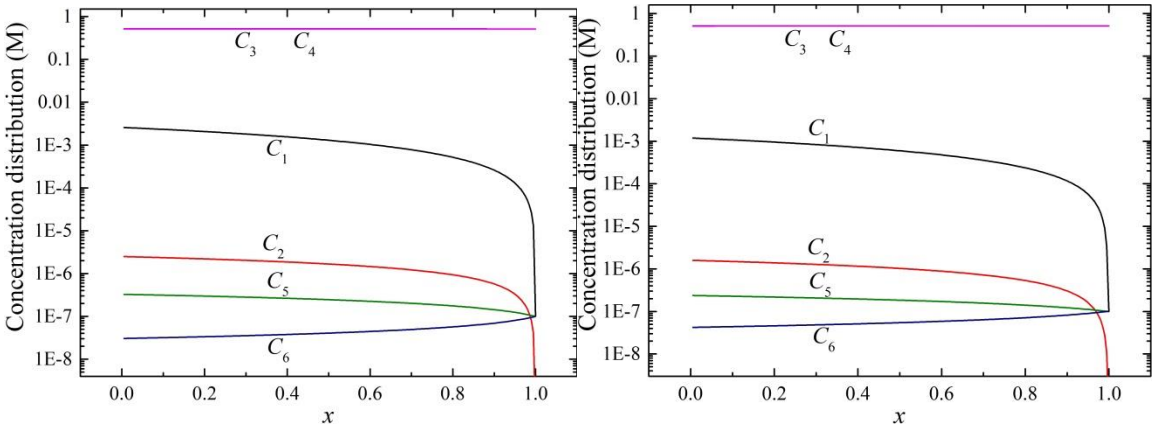
Concentration distribution (M)
x
C_1
C_2
C_3
C_4
C_5
C_6

(c) (d)

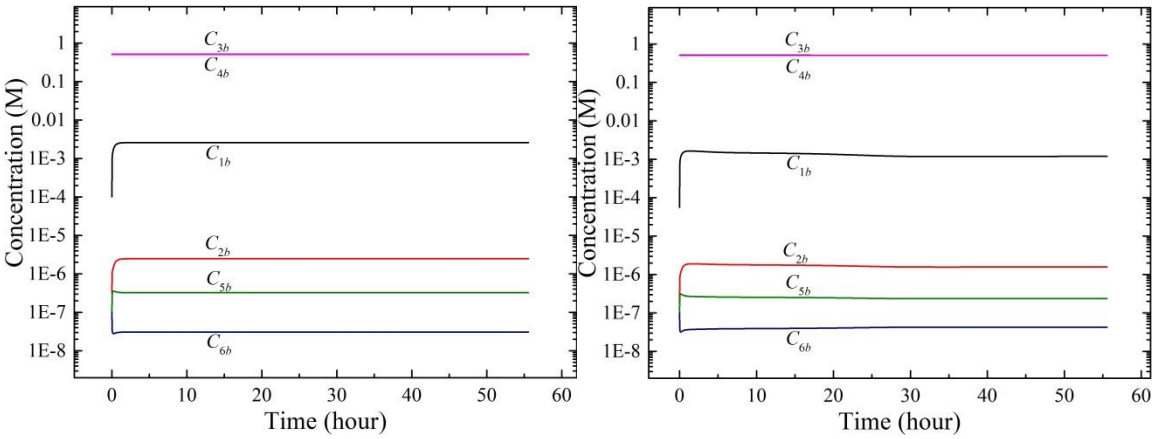
Concentration (M)
Time (hour)
C_{1b}
C_{2b}
C_{3b}
C_{4b}
C_{5b}
C_{6b}

(e) (f)

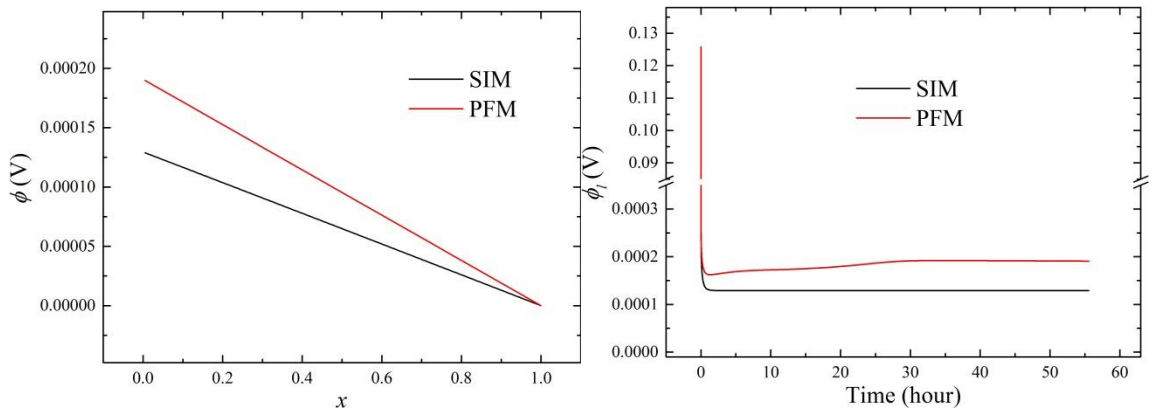

(g) (h)

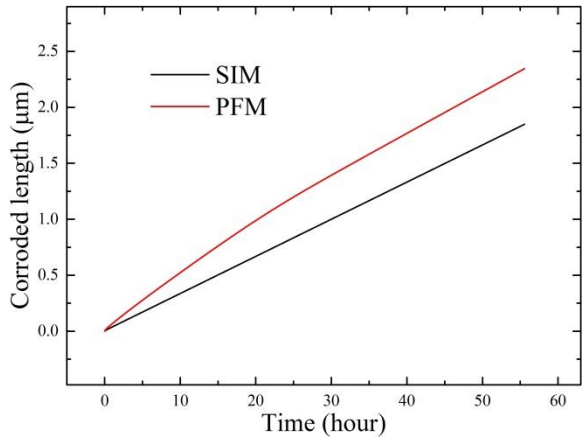

(i)

Fig. 2. The comparison of simulation results between SIM and PFM at ϕ_M = -0.4 *V*. (a), (c) and (e) are the results obtained by SIM. (b), (d) and (f) are obtained by the current PFM. (a) and (b) are the profiles of Fe^{2+}concentration, C_1 in the electrolyte at five different times. (c) and (d) are the distributions of six ion concentrations in the electrolyte at t=2×10^{5}s (55.56 hours). (e) and (f) are the evolution of six ion concentrations close to metal surface, C_{ib}, in the electrolyte. (g) shows the distributions of electric potential in the electrolyte at t=2×10^{5}s (55.56 hours) obtained by SIM and PFM. (h) is the evolution of electric potential

ϕ_l obtained by the two methods. And (i) is the corroded depth versus time from the two models.

Fig. 2(a) and (b) show the concentration profiles of Fe^{2+}, C_1, in the electrolyte obtained by SIM and PFM at five different times, respectively, which indicates that a steady state distribution of Fe^{2+} is reached at $t = 10^4$s. Fig. 2(c) and (d) show the concentration distributions of six ion species in logarithmic scale in the electrolyte at the time of 2×10^5 seconds (55.56 hours) obtained by SIM and PFM, respectively. The concentration of H^+, C_5, is higher at crevice tip than at the mouth, and the profiles of C_5 and C_6 are symmetric with respect to the value of 10^{-7}M. The higher C_5 at the crevice tip is mainly the consequence of higher tip C_1 via the hydrolysis of metal ion Fe^{2+} [see Eq. (1)] or the reaction terms in the Eqs. (3) and (4), which produces a strong coupling among C_1, C_2 and C_5. Comparing to the H^+ produced by the hydrolysis of Fe^{2+}, the depletion of H^+ from electrolyte via the reduction of H^+ at the electrode [see Eq. (40)] and its recombination with OH^- [see Eq. (2)] is very small. Thus, the higher overpotential causes a higher corrosion rate and higher C_1 and C_5 in the electrolyte. This relation between overpotential and concentration of H^+, C_5, will be discussed in a later section. The mirror symmetry of H^+, C_5, and OH^-, C_6, concentration profiles with respect to the value of 10^{-7}M is associated with the dissociation of water or the reaction terms in Eqs. (7) and (8). The pH values close to the metal surface obtained by SIM and PFM are 6.49 and 6.63, respectively. The concentrations of Cl^-, C_3, and Na^+, C_4, are very high and are similar. The reason is that the system we studied is iron immersed into a 3% $NaCl$ solution, which corresponds to a concentration of 0.513 M. Compared to the concentration of the salt water, the concentrations of other species are very low. For example, the concentration of Fe^{2+} close

to metal surface in the electrolyte, C_{1b}, is on the order of 10^{-3}M, due to the slow release speed from metal surface and the fast transportation of Fe^{2+} to the crevice mouth under the driving force of the concentration gradient and the electric field.

Fig. 2(e) and (f) show the concentration evolution of six species close to the metal surface in the electrolyte with time. The initial concentrations are from the equilibrium values determined by Eqs. (12), (13) and the charge neutrality condition. After a short period of time, they all reach the steady state values. It is found that the Eqs. (12), (13) and the charge neutrality condition are satisfied. For instance, the values of $C_{2b}C_{5b}/C_{1b}$ obtained by SIM and PFM at time 55.55 hours are 3.13×10^{-10}M and 3.11×10^{-10}M, respectively, which are very close to the value of K_1, 3.16×10^{-10}M. And $C_{5b}C_{6b}$ obtained by both models is 10^{-14} $(\text{M})^2$, same as K_2.

Fig. 2(g) shows the electric potential distribution in the electrolyte obtained by SIM and PFM, which correspond to electric field strength of 0.065V/m and 0.09V/m, respectively. The electric potential close to metal surface is higher than that in the other regions in the electrolyte. This is because that the metal ion, Fe^{2+} dissolving into the solution leads to a temporary slight increase of positive charges from zero at the vicinity of the metal surface in the electrolyte, which further leads to a higher electric potential at the vicinity of metal surface, ϕ_l. This temporary slight charge increase will be neutralized very quickly by the Cl^- migrating from crevice mouth due to the strong electric force, which maintains electroneutrality. The evolution of ϕ_l with time is shown in Fig. 2(h), which decreases at initial period and reaches a steady value later.

Based on Fig. 2(i), the average corrosion rates obtained by SIM and PFM are 2.91×10^{-4}m/year and 3.7×10^{-4}m/year, respectively. The concentration polarization overpotential, η_c, and the total overpotential, η_a, change with time due to the variation of C_{1b} and ϕ_l during the corrosion process. After 55.56 hours of corrosion, the concentration polarization overpotentials (η_c) calculated from SIM and PFM are -7.65×10^{-2}V and -8.64×10^{-2}V and the total overpotentials (η_a) are 0.116V and 0.126V, respectively. We can find that there are some discrepancies between the results obtained by SIM and PFM. The main reason is that the movement of metal-electrolyte interface in PFM is determined by the mobility which is influenced by the total overpotential. Some parameters such as C_{1b} and ϕ_l have to be determined in PFM by selecting a point near the interface, which can influence the concentration overpotential and the total overpotential through Eqs. (24) and (25), and further influence the mobility of metal-electrolyte interface via Eqs. (23) and (26). In principle, one can minimize the differences through fine tuning these parameters in PFM.

3.2 Corrosion behavior under different metal potentials

This section discusses the corrosion behavior under different metal potentials. Fig. 3 shows the composition profile of metal ions under four different metal potentials at t=0 and t = 55.56 hours obtained by PFM.

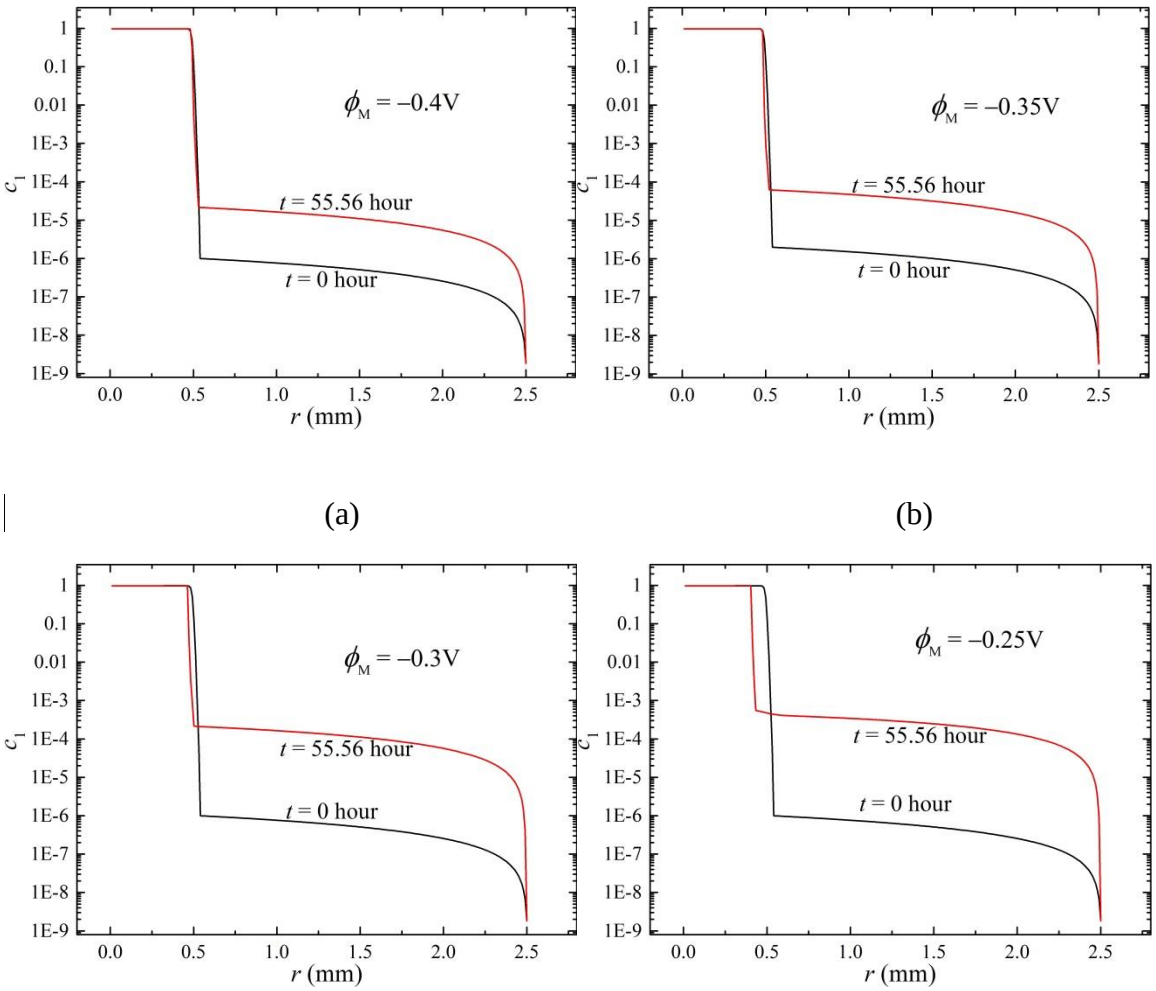

Fig. 3. Profiles of c_1 in log scale under four metal potentials ϕ_M obtained by PFM.

The interface recedes into the metal portion with different lengths that correspond to the corroded lengths under different metal potentials for the same time interval 55.56 hours. It shows that an increased metal potential results in higher corrosion rate. The composition of Fe^{2+}, c_1, close to interface in the electrolyte increases with the metal potential. The electrochemical quantities at crevice tip versus metal potentials obtained by SIM and PFM are shown in Fig. 4.

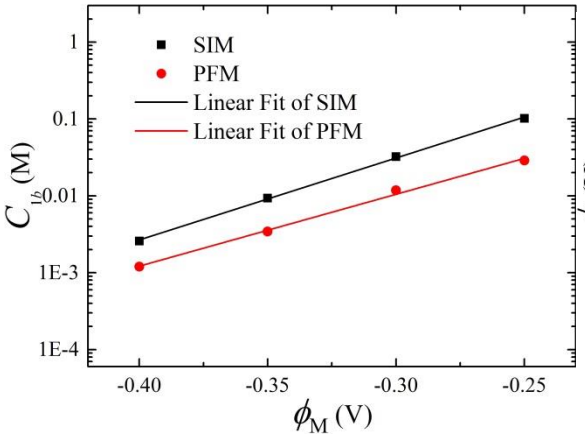
SIM
PFM
Linear Fit of SIM
Linear Fit of PFM
$C_{1/2}$ (M)
ϕ_M (V)

(a)

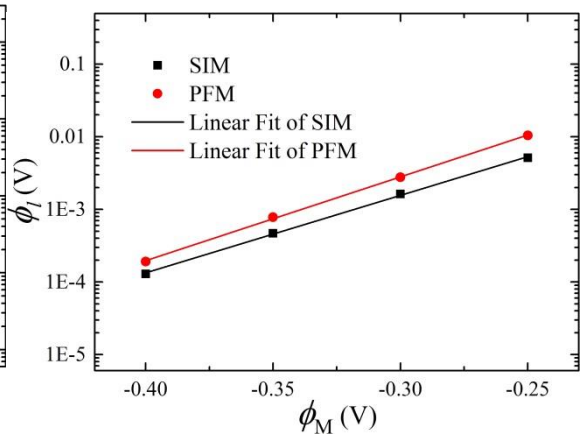
SIM
PFM
Linear Fit of SIM
Linear Fit of PFM
ϕ_l (V)
ϕ_M (V)

(b)

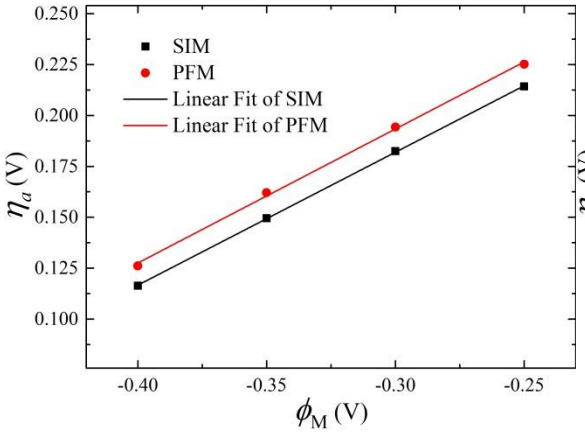
SIM
PFM
Linear Fit of SIM
Linear Fit of PFM
η_a (V)
ϕ_M (V)

(c)

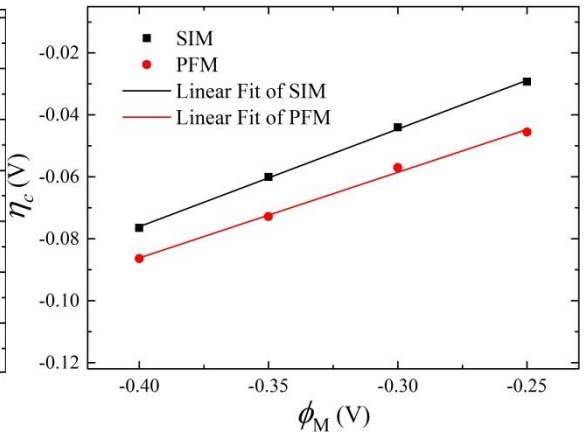
SIM
PFM
Linear Fit of SIM
Linear Fit of PFM
η_c (V)
ϕ_M (V)

(d)

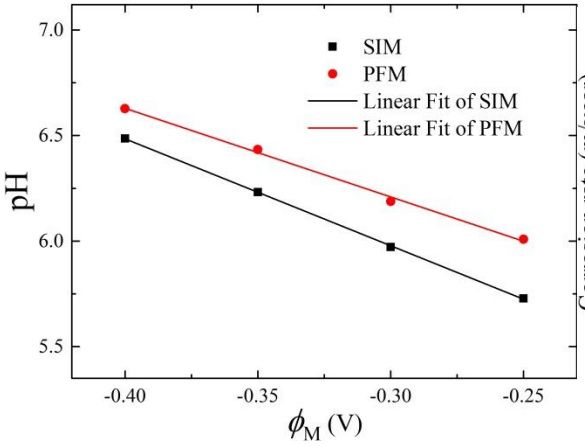
SIM
PFM
Linear Fit of SIM
Linear Fit of PFM
pH
ϕ_M (V)

(e)

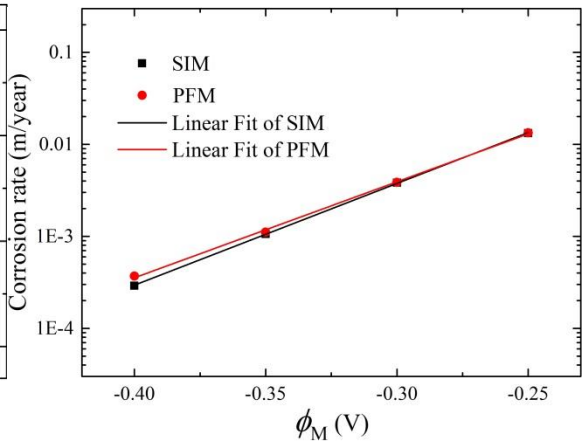
SIM
PFM
Linear Fit of SIM
Linear Fit of PFM
Corrosion rate (m/year)
ϕ_M (V)

(f)

Fig. 4. The corrosion rate, C_{1b}, ϕ_l, pH, η_a and η_c close to metal surface versus electric potential in the metal, ϕ_M, obtained by SIM and PFM at $t=2\times10^5 s$ (55.56 *hour*).

Fig. 4 shows the values of C_{1b}, ϕ_l, pH, η_a and η_c near the metal surface and corrosion rate versus ϕ_M, obtained by SIM and PFM, respectively. The results obtained by SIM and PFM show the same trend. According to Eq. (25), the value of η_c is smaller than zero because the concentration of Fe^{2+}, C_1, near the metal surface is smaller than 1M. It is observed that C_{1b}, ϕ_l, η_a and corrosion rate increase with ϕ_M, but pH and the absolute value of η_c decreases with ϕ_M, resulting from the increase of dissolution rate of the metal due to larger overpotential by increasing ϕ_M. The larger dissolution rate of metal leads to relatively larger flow of Fe^{2+} into the solution through the metal surface, which leads to larger C_{1b}, ϕ_l and η_a. The pH decreases linearly with the increase of ϕ_M, meaning that a faster corrosion rate will lead to stronger acidity at the crevice tip. The relations for C_{1b}, ϕ_l and corrosion rate versus ϕ_M are nonlinear, while the relation between logarithm of them and ϕ_M is linear. According to the Butler-Volmer equation (23), the relation between the flux of Fe^{2+} from metal into electrolyte, j_1, and the total overpotential, η_a, is $j_1 \propto \exp(\eta_a)$, because the opposite process (deposition of metal ion onto the electrode) is very small and can be ignored. The above simulations were done using the same value of D_{1r} determined in section 3.1. It shows that the effective interfacial diffusivity determined by the expressions (22) and (26) can well describe the interface velocity in the whole range of simulation conditions. The predicted corrosion rates under ϕ_M from -0.4V to -0.25V are the same order of magnitude as the experimental results on mild steel in deaerated 3% *NaCl* solution at 298K [50] as shown in Fig. 5. The increases of C_{1b}, ϕ_l and corrosion rate are about 4 times in SIM and

PFM for every increase of 0.05 V in ϕ_M, which is also consistent with the results observed in the experiment [50] as shown in Fig. 5.

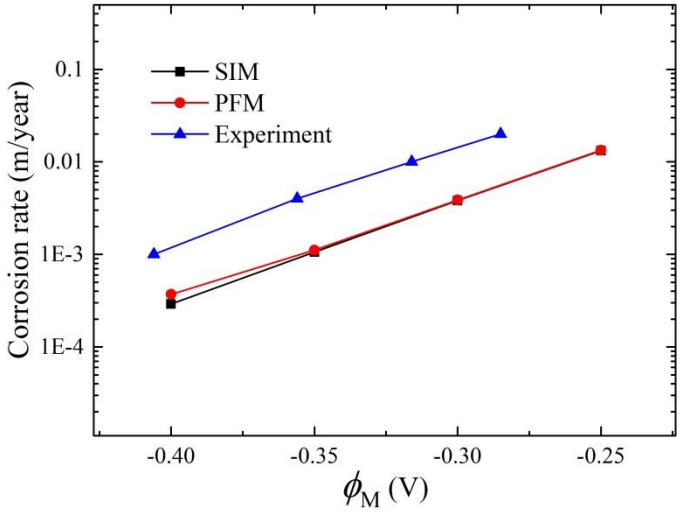

Fig. 5. The corrosion rate versus electric potential in the metal, ϕ_M, obtained by SIM, PFM at t=2×10^{5}s (55.56 hour), and experiment [50]. The experiment data are extracted from Fig. 47.1 in Ref. [50].

The difference between the corrosion rates under different metal potentials obtained by SIM and PFM is very small. And slopes by the three methods are almost the same. There still are some discrepancies between the results obtained by the experiment and theoretical modeling (PFM and SIM). The reason is that the crevice length and the ions concentrations at the crevice mouth in the experiment are unknown. They will influence the ions concentrations C_{ib} (i = 1, 2, ···, 6) and the electric potential, ϕ_l, close to interface in the electrolyte, and further influence crevice corrosion rates. In addition, in SIM and PFM, it is assumed that only the crevice tip is under corrosion and crevice wall is protected by passive films. However, in the experiment, the geometry of crevice is more complex and part of crevice wall may be under corrosion due to incomplete passivation.

The corrosion rate, concentration of ion species and electric potential in the electrolyte are several orders smaller than those results obtained by Sharland [6]. Sharland has mentioned that his results "are unrealistically high which would suggest that some of the approximations made in the construction of the model may not be valid" [6].

4. Conclusions

A quantitative PFM for crevice corrosion of steels in a sodium chloride solution is developed. The model accounts for the transport of six types of ions in the electrolyte and the evolution of electrochemical potential. The simulation results from this model are compared to those from a SIM. Both PFM and SIM models are used to study the distributions of the six types of ions, pH value, electrostatic potential, and corrosion rate as a function of time in one dimension. The results from the developed PFM show the same trend and are within the same magnitude as those from SIM. The corrosion rates predicted by both models are in good agreement with experimental results. The PFM does not need to track the interface position and apply interface conditions explicitly, and does not require complicated numerical scheme for dealing with the moving interface that normally required in SIM. In order to take full advantage of PFM, it is suggested that for 2D and 3D corrosion modeling the modeling domain should be the same for all ionic species, that is, the domain should include the corroding metal and the electrolyte. For those ionic species that exist only in the electrolyte, one can assign small mobility for these ions in metal. Therefore, PFM has great potential to study many corrosion related phenomena. This work provides a good foundation for further study on 2D and 3D localized corrosion with or without insoluble corrosion products using phase-field methods. When the concentrations

of some species in the electrolyte exceed the saturation limits, some insoluble products may precipitate on the wall of crevice. The formation of precipitates can be treated as new phases, which will require the introduction of new order parameters and their governing equations into the model.

Acknowledgement

This work was supported by Research Grants Council of Hong Kong (PolyU 152140/14E) and the National Natural Science Foundation of China (No.51271157).

Appendix A

Let

$$X(t) = L(t)x \tag{A.1}$$

where, $0 \le x \le 1$, L(t) changes with time. Then, $dX(t) = L(t)dx + xdL(t)$ and

$$\frac{\partial x}{\partial X} = \frac{1}{L(t)} \tag{A.2}$$

$$\frac{\partial X(t)}{\partial t} = L(t)\frac{\partial x}{\partial t} + x\frac{dL(t)}{dt} = x\frac{dL(t)}{dt} \tag{A.3}$$

Then,

$$\begin{aligned}\frac{dc_1(X,t)}{dt} &= \frac{\partial c_1(X,t)}{\partial t} + \frac{\partial X}{\partial t}\frac{\partial c_1(r,t)}{\partial X} = \frac{\partial c_1(X,t)}{\partial t} + \frac{\partial X}{\partial t}\frac{dx}{dX}\frac{\partial c_1(x,t)}{\partial x} \\ &= \frac{\partial c_1(x,t)}{\partial t} + \frac{dL}{dt}\frac{x}{L}\frac{\partial c_1(x,t)}{\partial x}\end{aligned} \tag{A.4}$$

and substituting above Eqs. (A.2) - (A.4) into Eq. (3) gets

$$\frac{\partial c_1(x,t)}{\partial t}+\frac{x}{L}\frac{dL}{dt}\frac{\partial c_1(x,t)}{\partial x}=\frac{D_1}{L^2}\frac{\partial^2 c_1(x,t)}{\partial x^2}+\frac{z_1 D_1 F}{RTL^2}\frac{\partial}{\partial x}\left(c_1\frac{\partial \phi(x,t)}{\partial x}\right)-k_{1F}c_1+k_{1B}c_2c_5/V_m \quad \text{(A.5)}$$

The coordinate transformations for equations of other ion species are similar.

Appendix B

The n-degree interpolation polynomial in the Lagrange form is

$$L_k(x)=\sum_{j=0}^{k} f(x_j)l_j(x) \quad \text{(B.1)}$$

where, $l_j(x)=\prod_{\substack{i=0\\ i\neq j}}^{k}\frac{x-x_i}{x_j-x_i}$, j= 0, 1, ⋯, k. $f(x_j)$ is the value of function f at grid x_j.

Here, for the simplicity. We only use one-degree Lagrange polynomial to do piecewise interpolation. The Lagrange polynomial basis is

$$l_0(x)=\frac{x-x_1}{x_0-x_1}, l_1(x)=\frac{x-x_0}{x_1-x_0} \quad \text{(B.2)}$$

There is a fixed number of grids in electrolyte in SIM, n_x = 200. The number of grids in electrolyte in PFM (n_{xl}) varies with the corrosion process, and $n_{xl} \geq n_x$. The values of c_1 in PFM grids should be mapped onto SIM grids.

$$c_1(i)=c_1(j)l_0(x_i)+c_1(j+1)l_1(x_i) \quad \text{(B.3)}$$

where i= 1, ⋯, n_x, $l_0(x_i)=\frac{x_i-x_1}{x_0-x_1}$, $l_1(x_i)=\frac{x_i-x_0}{x_1-x_0}$, $\Delta x=n_{xl}/n_x$, $x_i=i\times\Delta x$, $j=\text{int}(x_i)$ which is the integer part of x_i with $j\leq x_i$, $x_0=j$ and $x_1=j$+1. A reverse process is needed when mapping from SIM to PFM.

References:

[1] H.W. Pickering, Whitney Award Lecture-1985: On the Roles of Corrosion Products in Local Cell Processes, Corrosion, 42 (1986) 125-140.
[2] B. De Force, H. Pickering, A clearer view of how crevice corrosion occurs, JOM, 47 (1995) 22-27.
[3] J.W. Oldfield, W.H. Sutton, Crevice Corrosion of Stainless Steels: I. A Mathematical Model, British Corrosion Journal, 13 (1978) 13-22.
[4] A. Turnbull, J. Thomas, A model of crack electrochemistry for steels in the active state based on mass transport by diffusion and ion migration, Journal of the Electrochemical Society, 129 (1982) 1412-1422.
[5] A. Turnbull, D.H. Ferriss, Mathematical modelling of the electrochemistry in corrosion fatigue cracks in structural steel cathodically protected in sea water, Corrosion Science, 26 (1986) 601-628.
[6] S.M. Sharland, P.W. Tasker, A mathematical model of crevice and pitting corrosion—I. The physical model, Corrosion Science, 28 (1988) 603-620.
[7] S.M. Sharland, A mathematical model of crevice and pitting corrosion—II. The mathematical solution, Corrosion Science, 28 (1988) 621-630.
[8] S.M. Sharland, C.P. Jackson, A.J. Diver, A finite-element model of the propagation of corrosion crevices and pits, Corrosion Science, 29 (1989) 1149-1166.
[9] S.M. Sharland, A review of the theoretical modelling of crevice and pitting corrosion, Corrosion Science, 27 (1987) 289-323.
[10] J.C. Walton, G. Cragnolino, S.K. Kalandros, A numerical model of crevice corrosion for passive and active metals, Corrosion Science, 38 (1996) 1-18.
[11] R. Kelly, K. Stewart, M. Ives, B. MacDougall, J. Bardwell, Combining the ohmic drop and critical crevice solution approaches to rationalize intermediate attack in crevice corrosion, Passivity of Metals and Semiconductors VIII, eds. MB Ives, BR MacDougall, JA Bardwell, PV, (2001) 99-42.
[12] G.F. Kennell, R.W. Evitts, K.L. Heppner, A critical crevice solution and IR drop crevice corrosion model, Corrosion Science, 50 (2008) 1716-1725.
[13] J. Xiao, S. Chaudhuri, Predictive modeling of localized corrosion: An application to aluminum alloys, Electrochimica Acta, 56 (2011) 5630-5641.
[14] S. Sarkar, J.E. Warner, W. Aquino, A numerical framework for the modeling of corrosive dissolution, Corrosion Science, 65 (2012) 502-511.
[15] Z. Chen, F. Bobaru, Peridynamic modeling of pitting corrosion damage, Journal of the Mechanics and Physics of Solids, 78 (2015) 352-381.
[16] Z. Chen, G. Zhang, F. Bobaru, The Influence of Passive Film Damage on Pitting Corrosion, Journal of The Electrochemical Society, 163 (2016) C19-C24.
[17] R. Duddu, Numerical modeling of corrosion pit propagation using the combined extended finite element and level set method, Computational Mechanics, 54 (2014) 613-627.
[18] R. Duddu, N. Kota, S.M. Qidwai, An Extended Finite Element Method Based Approach for Modeling Crevice and Pitting Corrosion, Journal of Applied Mechanics, 83 (2016) 081003-081003-081010.

[19] Y. Onishi, J. Takiyasu, K. Amaya, H. Yakuwa, K. Hayabusa, Numerical method for time-dependent localized corrosion analysis with moving boundaries by combining the finite volume method and voxel method, Corrosion Science, 63 (2012) 210-224.
[20] K. Amaya, S. Aoki, Effective boundary element methods in corrosion analysis, Engineering Analysis with Boundary Elements, 27 (2003) 507-519.
[21] S. Aoki, K. Kishimoto, Prediction of galvanic corrosion rates by the boundary element method, Mathematical and Computer Modelling, 15 (1991) 11-22.
[22] F.E. Varela, Y. Kurata, N. Sanada, The influence of temperature on the galvanic corrosion of a cast iron-stainless steel couple (prediction by boundary element method), Corrosion Science, 39 (1997) 775-788.
[23] W. Sun, L. Wang, T. Wu, G. Liu, An arbitrary Lagrangian–Eulerian model for modelling the time-dependent evolution of crevice corrosion, Corrosion Science, 78 (2014) 233-243.
[24] L.Q. Chen, Phase-field models for microstructure evolution, Annual Review of Materials Science, 32 (2002) 113-140.
[25] W.J. Boettinger, J.A. Warren, C. Beckermann, A. Karma, Phase-field simulation of solidification, Annual Review of Materials Science, 32 (2002) 163-194.
[26] J.E. Guyer, W.J. Boettinger, J.A. Warren, G.B. McFadden, Phase field modeling of electrochemistry. I. Equilibrium, Physical Review E, 69 (2004) 021603.
[27] J.E. Guyer, W.J. Boettinger, J.A. Warren, G.B. McFadden, Phase field modeling of electrochemistry. II. Kinetics, Physical Review E, 69 (2004) 021604.
[28] W. Gathright, M. Jensen, D. Lewis, Phase field model of chemical reactions with an example of a solid electrolyte gas sensor, Electrochemistry Communications, 13 (2011) 520-523.
[29] W. Gathright, M. Jensen, D. Lewis, A phase field model of electrochemical impedance spectroscopy, Journal of Materials Science, 47 (2012) 1677-1683.
[30] W. You-Hai, C. Long-Qing, A.H. Jeffrey, Phase-field modeling of corrosion kinetics under dual-oxidants, Modelling and Simulation in Materials Science and Engineering, 20 (2012) 035013.
[31] F. Yang, D.-N. Fang, B. Liu, A theoretical model and phase field simulation on the evolution of interface roughness in the oxidation process, Modelling and Simulation in Materials Science and Engineering, 20 (2012) 015001.
[32] T.-L. Cheng, Y.-H. Wen, J.A. Hawk, Diffuse-Interface Modeling and Multiscale-Relay Simulation of Metal Oxidation Kinetics—With Revisit on Wagner's Theory, The Journal of Physical Chemistry C, 118 (2014) 1269-1284.
[33] F. Yang, B. Liu, D.-n. Fang, Analysis on high-temperature oxidation and growth stress of iron-based alloy using phase field method, Applied Mathematics and Mechanics, 32 (2011) 757-764.
[34] A.C. Powell, Y. Shibuta, J.E. Guyer, C.A. Becker, Modeling electrochemistry in metallurgical processes, JOM, 59 (2007) 35-43.
[35] D. Dussault, A.C. Powell, Phase field modeling of electrolysis in a slag or molten salt, in: Proc. Mills Symp, 2002, pp. 359-371.
[36] A. Hamid, Phase-field modelling of electro-deoxidation in molten salt, Modelling and Simulation in Materials Science and Engineering, 14 (2006) 963.
[37] Y. Shibuta, Y. Okajima, T. Suzuki, A phase-field simulation of bridge formation process in a nanometer-scale switch, Scripta materialia, 55 (2006) 1095-1098.

[38] S. Yasushi, O. Yoshinao, S. Toshio, Phase-field modeling for electrodeposition process, Science and Technology of Advanced Materials, 8 (2007) 511.
[39] W. Pongsaksawad, A.C. Powell, D. Dussault, Phase-field modeling of transport-limited electrolysis in solid and liquid states, Journal of The Electrochemical Society, 154 (2007) F122-F133.
[40] A. Powell, W. Pongsaksawad, Phase field modeling of phase boundary motion due to transport-limited electrochemical reactions, WIT Transactions on Engineering Sciences, 54 (2007).
[41] W. Mai, S. Soghrati, R.G. Buchheit, A phase field model for simulating the pitting corrosion, Corrosion Science, 110 (2016) 157-166.
[42] W. Mai, S. Soghrati, A phase field model for simulating the stress corrosion cracking initiated from pits, Corrosion Science, 125 (2017) 87-98.
[43] W. Mai, S. Soghrati, New phase field model for simulating galvanic and pitting corrosion processes, Electrochimica Acta, 260 (2018) 290-304.
[44] R.G. Kelly, J.R. Scully, D. Shoesmith, R.G. Buchheit, Electrochemical techniques in corrosion science and engineering, CRC Press, 2002.
[45] J.O.M. Bockris, D. Drazic, A.R. Despic, The electrode kinetics of the deposition and dissolution of iron, Electrochimica Acta, 4 (1961) 325-361.
[46] F. Pagnanelli, M. Luigi, S. Mainelli, L. Toro, Use of natural materials for the inhibition of iron oxidizing bacteria involved in the generation of acid mine drainage, Hydrometallurgy, 87 (2007) 27-35.
[47] C.F. Baes, R.E. Mesmer, The hydrolysis of cations, Wiley, New York, 1976.
[48] M. Eigen, L. de Maeyer, Self-Dissociation and Protonic Charge Transport in Water and Ice, Proceedings of the Royal Society of London. Series A. Mathematical and Physical Sciences, 247 (1958) 505-533.
[49] F.H. Stillinger, Proton transfer Reactions and kinetics in Water, Theoretical Chernistry: Advances and Perspectives; Eyring, H., Henderson, D., Eds, 3 (1978) 177-234.
[50] R.W. Revie, H.H. Uhlig, Uhlig's corrosion handbook, John Wiley & Sons, 2011.